energies

Article

Transient Simulation of the Six-Inlet, Two-Stage Radial Turbine under Pulse-Flow Conditions

Dariusz Kozak * and Paweł Mazuro

Department of Aircraft Engines, Faculty of Power and Aeronautical Engineering, Institute of Heat Engineering, Warsaw University of Technology, 00-665 Warsaw, Poland; pmazuro@itc.pw.edu.pl
* Correspondence: dariusz.kozak.dokt@pw.edu.pl; Tel.: +48-509-679-182

Abstract: In recent years, the automotive sector has been focused on emission reductions using hybrid and electric vehicles. This was mainly caused by political trends promoting "green energy". However, that does not mean that internal combustion engines (ICEs) should be forgotten. The ICE has still the potential of recovering energy from exhaust gases. One of the promising ways to recover energy is turbocharging. Over the years engine manufacturers have designed very efficient turbocharger systems which have greatly increased the overall engine efficiency. This led to pollutant emission reductions. This paper presents the results of the three-dimensional (3-D) numerical simulations of the two-stage, six-inlet turbocharging system under the influence of unsteady, pulsed-flow conditions. The calculations were carried out for three turbine speeds. The most interesting results of this study were the separation of exhaust gases coming from the six-exhaust pipes and the performance of both stages under pulse-flow conditions. The two-stage turbocharging system was compared against the single-stage turbocharging system and the results showed that the newly designed two-stage turbine system properly separated the exhaust gases of the adjacent exhaust pipes.

Keywords: two-stage turbocharger; internal combustion engine; gas separation; computational fluid dynamic; rotor

Citation: Kozak, D.; Mazuro, P. Transient Simulation of the Six-Inlet, Two-Stage Radial Turbine under Pulse-Flow Conditions. *Energies* **2021**, *14*, 2043. https://doi.org/10.3390/en14082043

Academic Editor: Francesco Balduzzi

Received: 28 January 2021
Accepted: 2 April 2021
Published: 7 April 2021

1. Introduction

The increasing trend of pollutant emissions reduction has forced engine manufacturers to focus their interest on hybrid and electric vehicles. The advantages of such vehicles are their relatively low fuel consumption and the possibility to recover energy. However, that does not mean that internal combustion engines (ICEs) should be eliminated from commercial use. One of the most important advantages of the ICE over electrically driven vehicles is the range. The limited battery charge of electric vehicles greatly constrains their maximal driving range. There are a lot of places in the ICE that can be improved to recover more energy from the exhaust gases. The hot exhaust gases contain a large portion of the energy that could be recovered with exhaust after-treatment components such as turbochargers which are driven by the hot exhaust gases from the cylinder. The first turbochargers had a single-stage rotor. However, the need for further energy recovery led to the implementation of multi-stage turbochargers. This has led to a greater energy recovery but on the other hand, also made the exhaust systems more complicated. Nowadays, two-stage turbocharging systems are used in ICEs. In such a system, the recovered energy is used to boost the air pressure at the intake of the engine. An analytical approach based on the power balance between the turbine and compressor with minimum energy consumption offers a reliable way to optimize the two-stage turbocharging system [1]. Key parameters such as the total expansion ratio and the total pressure ratio are often used with an analytical predesigned model [2,3]. The analytical approach of a two-stage turbocharged engine with three bypass valves was also studied at different altitudes [4]. The results showed that the cylinder combustion pressure decreased with the increase of the altitude. The two-stage turbocharged system was also analyzed during the steady-state and transient engine response regimes [5]. The results showed an improved durability of the two-stage turbocharging system with the reduction of the break-specific fuel consumption (BSFC) at low engine speeds. The analytical design of the Miller-cycle, two-stage turbocharging system leads to the reduction of the in-cylinder combustion temperature [6]. The 1-D simulations of series two-stage turbocharging systems allowed us to investigate the control of the pressure inside the exhaust system by the opening and closing of the variable guide vanes [7]. Researchers have shown that with the use of the 1-D simulations the displacement of the spark ignition V8, a two-stage turbocharged engine's pressure can be lowered by 20% without reducing the brake torque [8]. Such simulations used a predictive knock model. The minimum BSFC criterion was also used with the 1-D simulations of the two-stage turbocharging system [9]. The results were very optimistic, indicating an increase in the brake power and a reduction in fuel consumption. The 1-D simulation of the engine performance, with the two-stage turbocharging system at different altitudes, showed a greater increase in the brake power and torque when compared to the single-stage turbocharger [10,11]. Such simulations neglect the pressure losses inside ducts caused by the vortices, however, the 1-D calculations are in good agreement with the experimental data and require less computational time. The more complex 3-D calculations require a lot of computational resources. To reduce computational time, the geometry of the problem can be simplified. Such calculations allow investigating a fully developed turbulent flow with the Reynolds-averaged Navier-Stokes solver [12]. Some computational solvers for multistage turbomachinery issues implement discrete turbulence models with coupled, mixing-plane boundary conditions [13]. Such an approach favors the simulations under steady-state conditions. A coupled 1-D and 3-D calculations are also performed [14]. The 1-D calculations are performed in order to establish inlet boundary conditions for the 3-D numerical model. Both 1-D and 3-D solvers can be run simultaneously or independently.

The turbocompounding system is a type of multi-stage turbine system and one of the approaches to recover energy from exhaust gases. In such a system, an auxiliary turbine is installed behind the turbocharger. The exhaust gases drive the turbocharger and the auxiliary turbine. The energy from the exhaust gases can be recovered mechanically or electrically [15,16]. The additional electrical energy generated by the electric turbocompounder can be used to supply the vehicle's electronic units or batteries. Turbocompounding systems are mostly used in heavy-duty engines, where the reduction of fuel consumption plays an important part. Such systems are often assisted by exhaust recirculation valves which reduce the NOx concentration [17]. The mechanical recovery system consists of the auxiliary turbine connected with the crankshaft via gear train and fluid coupling. The electrical recovery is based on the auxiliary turbine that drives the alternating current (AC) generator. The generated electric energy can be used to supply the battery.

A two-stage turbocharging system further increases the energy recovery of the exhaust gases. However, such systems are complex and require precise control over the position of the variable nozzle vanes. Another interesting fact is that the two-stage turbocharging system increases the backpressure in the exhaust duct thus leading to an increase in the pumping losses. This might affect the in-cylinder combustion process. The turbochargers of the two-stage system operate independently from each other. That is why the rotational speed of each stage is different. Also, very few works have dealt with the 3-D computational approach of such a system.

This paper presents the numerical 3-D modelling results of a six-inlet, two-stage radial inflow turbine under pulse-flow conditions. The novelty of this work is the description of a two-stage model with both rotors placed on the same shaft, thus operating with the same rotational speed. Also, the separation of the exhaust pulses was investigated by implementing a six-inlet housing. Such a two-stage system will be used as a turbocompound unit in the 2-stroke, 6-cylinder opposed piston (OP) engine which is being designed at the Warsaw University of Technology. The two-stage system will be connected mechanically to the engine crankshaft via a gear train and fluid coupling.

The paper is organized as follows. Section 2 presents the theoretical approach for the estimation of the key turbine operating parameters. A detailed description of the computational geometry, mesh, and simulation setup is provided in Section 3. Section 4 presents the results of the model validation against the experimental data. Section 5 presents the results with an in-depth discussion. The conceptual adaptation scheme of the two-stage turbine system for the OP engine is described in Section 6. The conclusions are given in Section 7.

2. Theory

The typical hot section of a turbocharger consists of the volute and turbine wheel. The volute might be vaneless or equipped with the nozzle guide vanes, however, most of the volutes are vaneless as they are cheaper, smaller, less complex, and easier to manufacture. However, for research purposes, the nozzle guide vanes were considered to accelerate hot exhaust gases before the rotor wheel.

Due to the rotational movement of the rotor wheel, the correlation between velocities in the turbine stage is represented by Equation (1):

$$\vec{w} = \vec{c} - u \qquad (1)$$

where w is the relative velocity, c is the absolute velocity and u is the linear velocity at the tip of the rotor blades. Figure 1 shows the turbine configurations with the following Sections: inlet, behind nozzle vanes, behind first-stage rotor wheel, behind second-stage nozzle vanes, and behind the second-stage rotor wheel which corresponds to the following indexes: 0–4.

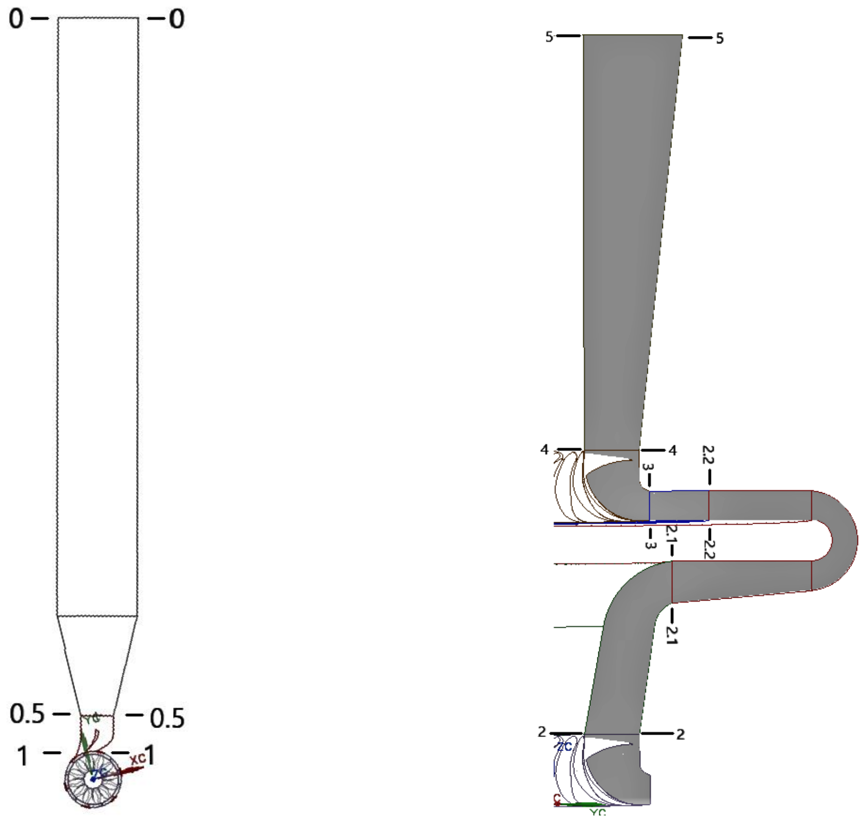

(**a**) (**b**)

Figure 1. Section numbers for: (**a**) the exhaust pipes and the first-stage nozzle guide vanes; (**b**) the first-stage rotor outlet, the inter-stage pipes, the second-stage nozzle vanes and the second-stage rotor outlet.

The pressure ratio at nozzle vanes of first and second-stage is calculated using Equations (2) and (3) [18]:

$$\frac{p_1}{p_0^*} = \left[1 - \frac{c_1^2}{2\varphi^2 \frac{k'}{k'-1} R' T_0^*}\right]^{\frac{k'}{k'-1}} \tag{2}$$

$$\frac{p_3}{p_2^*} = \left[1 - \frac{c_3^2}{2\varphi^2 \frac{k'}{k'-1} R' T_2^*}\right]^{\frac{k'}{k'-1}} \tag{3}$$

where p_1 and p_3 are the pressures behind the first and second-stage nozzle vanes, p_0^* and p_2^* are the total pressures before the first and second-stage nozzle vanes, T_0^* and T_2^* are the total temperatures before the first and second-stage nozzle vanes, c_1 and c_3 are the absolute velocities after nozzle vanes for both stages, φ is the vane flow coefficient, k' is the exhaust specific heat ratio, R' is the exhaust gas constant.

The temperature behind the nozzle vane at both stages can be calculated using Equations (4) and (5):

$$T_1 = T_0^* - \frac{c_1^2}{2\frac{k'}{k'-1} R'} \tag{4}$$

$$T_3 = T_2^* - \frac{c_3^2}{2\frac{k'}{k'-1} R'} \tag{5}$$

where T_1 and T_3 are the temperatures behind the first and second-stage nozzle vane.

Turbine isentropic enthalpy drop at the first and second-stage can be calculated using the following equation:

$$\Delta h_{Tiz}^{1,2} = \frac{c_{iz1,2}^2}{2} \tag{6}$$

where $c_{iz1,2}$ is the theoretical velocity during isentropic expansion from pressure p_0^* to pressure p_2 for the first-stage turbine and from the p_2^* to p_4 for the second-stage turbine. The reaction ratio ρ for both stages indicates rotor enthalpy drop compared to total enthalpy drop and it is calculated as:

$$\rho_{1,2} = \frac{\Delta h_{Wiz1,2}}{\Delta h_{Tiz} 1,2} \tag{7}$$

where $\Delta h_{Wiz1,2}$ is the rotor enthalpy drop. Indexes 1 and 2 represent the first and second-stage. The expansion work in rotor blades, as well as expansion efficiency for both stages, can be calculated with the equations:

$$l_{uT1} = u_1 c_{1u} \mp u_2 c_{2u} \tag{8}$$

$$l_{uT2} = u_3 c_{3u} \mp u_4 c_{4u} \tag{9}$$

$$\eta_{uT1,2} = \frac{l_{uT1,2}}{\Delta h_{Tiz1,2}} \tag{10}$$

Also, the total–static efficiency of both stages can be obtained using equations:

$$\eta_{T1} = \frac{h_0^* - h_2^*}{h_0^* - h_{2iz}} \tag{11}$$

$$\eta_{T2} = \frac{h_2^* - h_4^*}{h_2^* - h_{4iz}} \tag{12}$$

where h_0^* and h_2^* are total enthalpy at the inlet to the first and second-stage, h_2^*, h_{2iz}, h_4^* and h_{4iz} are total and isentropic enthalpies at the outlet of the first and second-stage.

The blade tip speed of both stages can be calculated using the formula:

$$u_{1,2} = \frac{D_{1,2}\pi n}{60} \tag{13}$$

where $D_{1,2}$ outer diameter of the turbine wheel. Index 1 stands for the first-stage rotor and 2 stands for the second-stage rotor.

3. Computational Approach

Figure 2a presents the B&W K44 turbine wheel which was used to create the 3-D model for the computational domain. The presented turbine wheel was scanned using the AKON smartSCAN 3D HE scanner and turntable. A total number of 60 scans per 360 degrees was done to scan as many surfaces as possible. However, the inter-blade zones were difficult to process, especially close to the hub. In those areas, computer-aided design software was used to create accurate surfaces. Table 1 shows the general parameters of the turbine wheel.

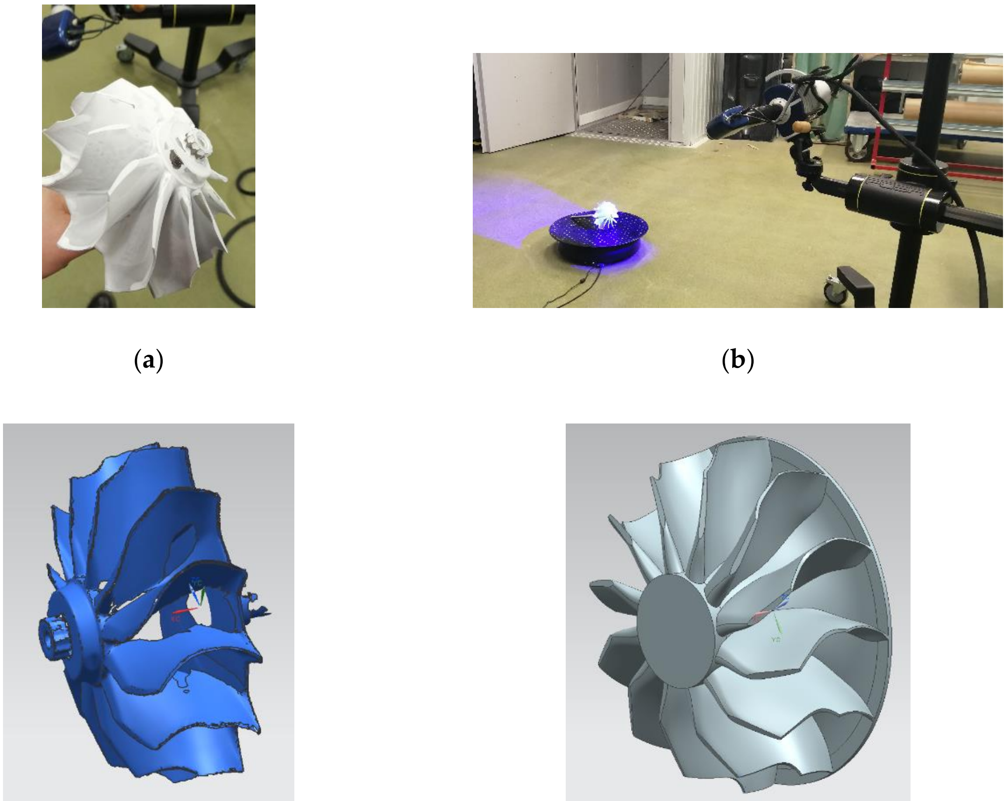

(**a**) (**b**)

(**c**) (**d**)

Figure 2. (**a**) The turbine rotor that was used for computational domain, (**b**) scanning process of the turbine wheel (**c**) the scanned geometry, (**d**) the generated 3-D model of the turbine wheel.

Figure 3a–c shows the set-up of the computational domain which consisted of nine domains: the exhaust pipes, the first-stage nozzle vanes, the first-stage turbine rotor, the tip clearance gap, the diffuser, the inter-stage pipes, the second-stage nozzle vanes (variable), the second-stage turbine rotor and the outlet. The same rotor geometry was used for the first and second-stage. The rotors were installed on a single shaft, thus the rotational velocity of the rotors was the same.

Table 1. The parameters of B&W K44 turbine wheel.

B&W K44 Turbine Wheel	
Type	Radial inflow
Number of blades	B&W K44
Inlet diameter [mm]	12
Outlet diameter [mm]	140
Inlet blade height [mm]	125
Outlet blade height [mm]	30

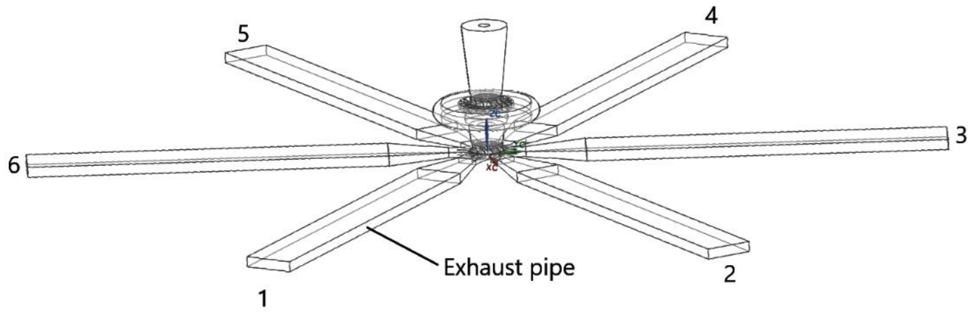

(**a**)

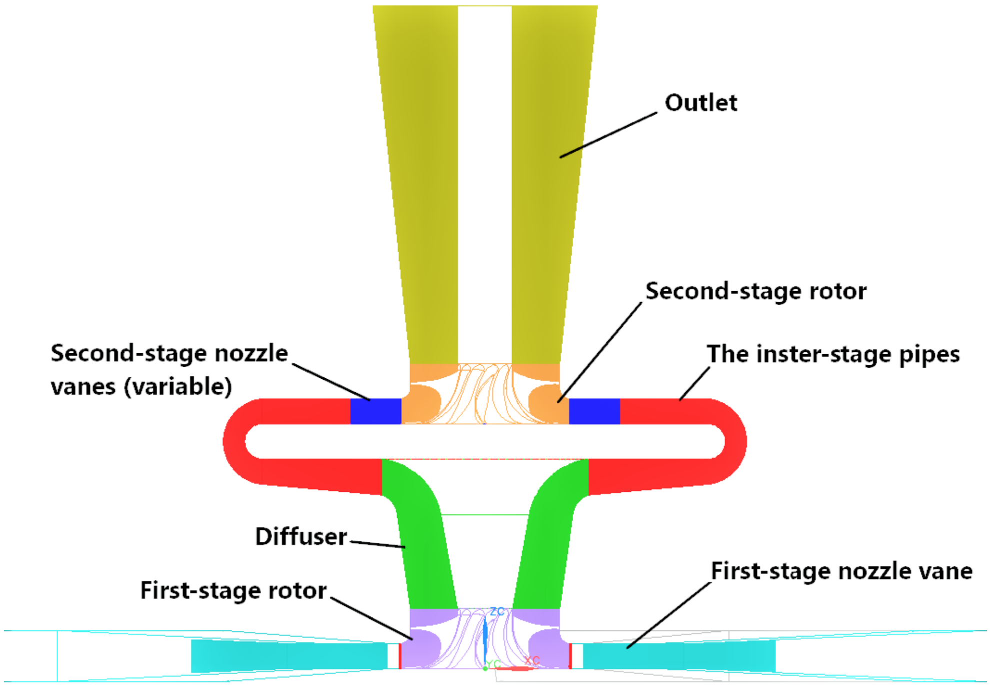

(**b**)

Figure 3. *Cont.*

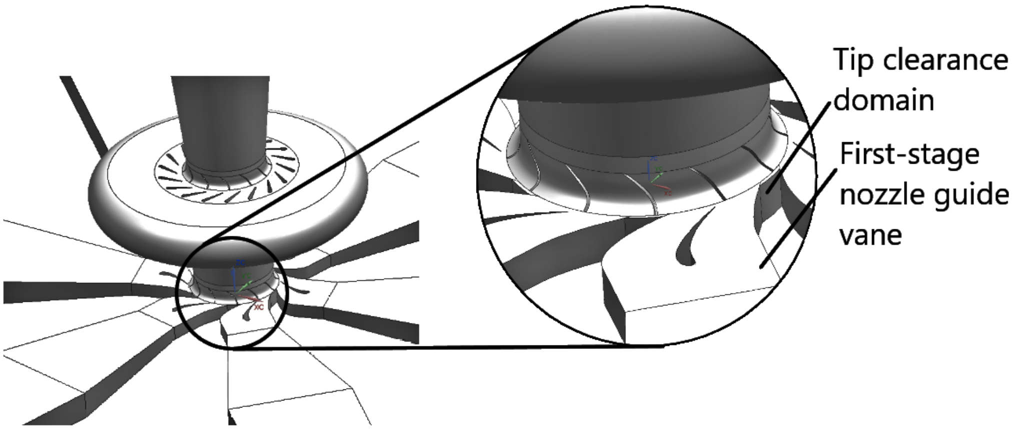

(**c**)

Figure 3. Computational domain set-up: (**a**) isometric view with 6 exhaust pipes; (**b**) cross-Section of the first and second-stage; (**c**) close-up at the clearance gap domain.

As can be seen from Figure 3a the six exhaust pipes are equally placed on the circumference of the first-stage rotor. The number of exhaust pipes corresponded to the number of engine cylinders. Each pipe transported the exhaust gases from the cylinder to the rotor. The hydraulic diameter of each exhaust pipe was 80 mm and the length was 1500 mm. The nozzle guide vanes were used to accelerate the exhaust gases before entering the first-stage rotor. The trailing edge (TE) angle of the nozzle vane was set to 30°. To investigate the leakage between the exhaust pipes during the pulse-flow, a small gap between the rotor blade tip and shroud was modeled and shown in Figure 3c. The height of the gap was set to 3 mm. To reduce the pressure losses between the two stages, the length and cross-Sectional area of the diffuser were iteratively adjusted. The inter-stage pipes consisted of the upstream straight segment, the elbow, and the downstream straight segment. The second-stage nozzle vanes consisted of 19 vanes and were fixed at the angle of 31°. The outlet domain was extended up to seven diameters of the second-stage rotor outlet.

A structured hexahedral mesh was generated on every domain except for the turbine rotor of the first and second stages. The ICEM CFD software was used for mesh generation. The rotor domains contained tetrahedral mesh which was later transformed into the polyhedral mesh in FLUENT. The mesh independence study of the rotor domains was performed before the beginning of the calculations. Figure 4 shows the plot of the volume-averaged total pressure values during the single revolution of the crankshaft for the different number of grid densities.

In order to inspect the mesh independence study for the transient issue, the total pressure values were investigated during the single revolution of the crankshaft. It was found that for the exhaust pipes the volume-average pressure plot remained almost unchanged for the number of the elements of 7200. For the first and second-stage rotor, the number of 1.34 million cells provided suitable pressure changes. The pressure changes inside the second-stage nozzle vanes remained unchanged with the number of 711,000 cells. Table 2 shows the number of cells for the rest of the domains.

Table 2. The number of cells for each domain.

Domain	Number of Elements
First-stage nozzle vane (x6)	18,036
Tip clearance gap (x6)	540
Inter-stage pipes	168,018
Outlet	374,850

As a result, the complete computational domain contained 2.1 million cells. Figure 5 shows the polyhedral mesh generated on the rotor domains.

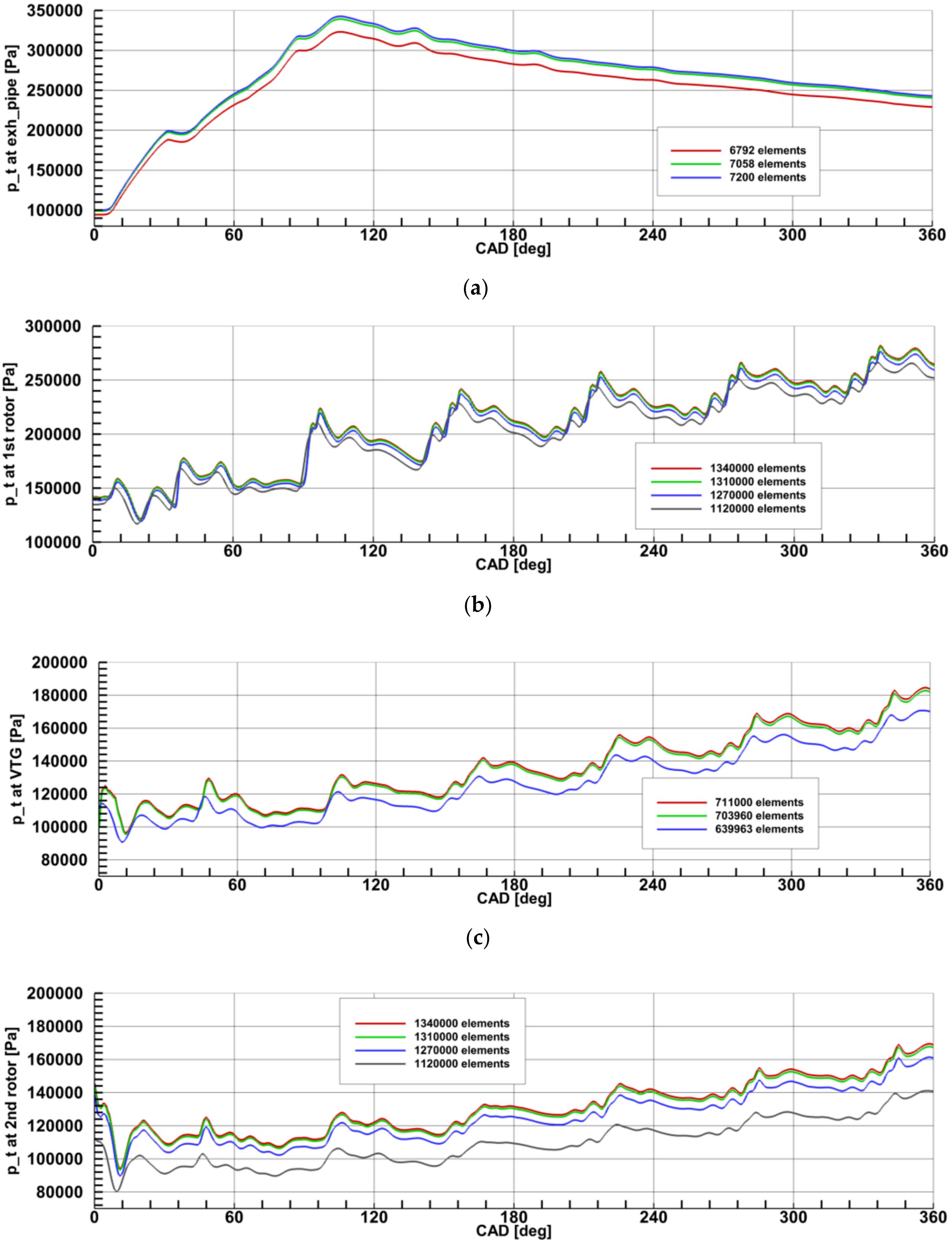

(**a**)

(**b**)

(**c**)

(**d**)

Figure 4. The total pressure plot against different number of elements during the single revolution of the crankshaft for the: (**a**) exhaust pipe, (**b**) first-stage rotor, (**c**) second-stage nozzle vanes, (**d**) second-stage rotor.

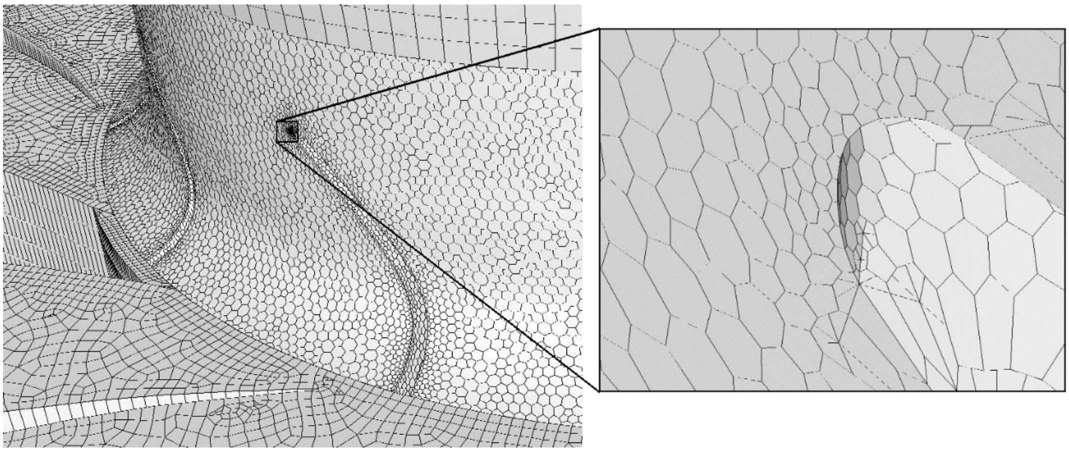

Figure 5. The polyhedral mesh generated on the rotor domain.

The ANSYS FLUENT software was used for transient simulations. For this reason, the sliding mesh method was used to capture the instantaneous parameters during the single time step. For the inlet of each exhaust pipe, the mass flow inlet boundary condition was set. The mass flow rate profile at the inlet to each exhaust pipe is shown in Figure 6.

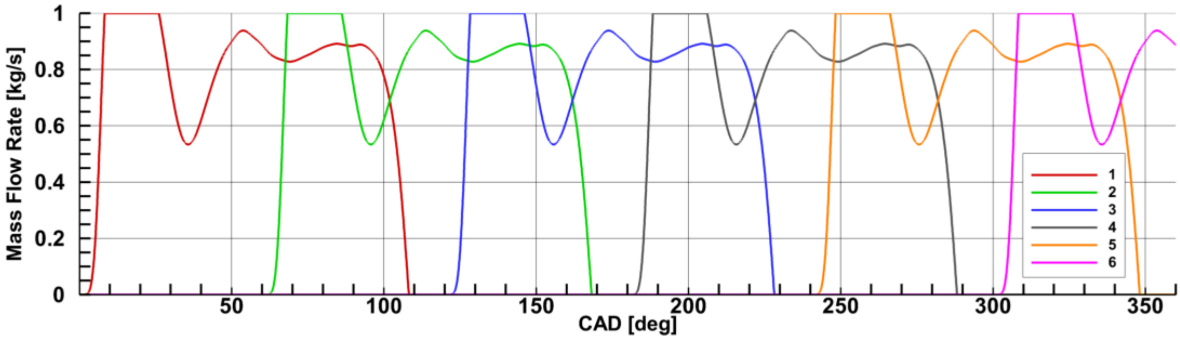

Figure 6. The inlet mass flow rate profile.

The mass flow rate profile was obtained from the 1-D, transient simulations of 6-cylinder, 1500 kW, 2-stroke engine. The rapid increase of the mass flow rate from 0 to 1 kg/s represented the beginning of the pulse-flow during the opening of the cylinder exhaust valve. The interval between the exhaust pulses was 60° which was adequate for the firing interval of the 6-cylinder, 2-stroke engine which parameters can be seen in Table 3. Table 4 shows the parameters of the boundary conditions.

To accurately capture the transient changes inside the whole exhaust system, a time step of 1.1×10^{-5} s was chosen. Such a time step was chosen due to the strongly warring cross-section and high velocity of the exhaust gases. Based on the previous simulations, such a small time step leads to stable calculations with the pressure-velocity coupling scheme. Each case was calculated using the single-equational Spalart-Allmaras (SA) turbulence model [19]. The SA turbulence model is based on the transport equation that is solved for a modified turbulent kinematic viscosity $\widetilde{\vartheta}$. The modified turbulent viscosity is assumed to be linear in near-wall region which greatly reduces computational time. Most of the turbomachinery simulations are done with k-ω shear stress transport or k-ε turbulence models. However, the SA model is also capable of capturing near-wall shockwave [20–22]. The SA model can also be extended for subsonic and transonic flows which also makes it suitable for capturing wake inside the stator domain [23]. Due to the linearization of the turbulent kinematic viscosity, the computational time is reduced [24]. The SA model tends to be more stable during calculations with the unstructured grid. With such a small time step size, the SA turbulence model greatly reduces the computational time.

Table 3. The operating parameters of the 6-cylinder, 2-stroke engine.

Engine Parameters	
Number of cylinders	6
Type	2-stroke
Rotational speed [rpm]	1500
Crankshaft angle step [deg]	0.1

Table 4. The parameters of the boundary conditions.

Inlet Boundary Conditions	
Type	Mass-flow-inlet
Mass flow rate [kg/s]	$0 \div 1$
Total temperature [K]	1100
Total pressure [Pa]	240,000.0
Outlet Boundary Conditions	
Type	Pressure-outlet
Outlet pressure [Pa]	100,000
Outlet temperature [K]	500

The calculations were carried out at the three different turbines rotational speed. Table 5 shows the defined operating points of both rotors and the blade tip speed, which was calculated with Equation (13).

Table 5. The turbine operating points with calculated blade tip speed.

n [rpm]	$u_{1,2}$ [m/s]
$60,000$	439.6
$50,000$	366.3
$40,000$	293.1

The calculations were carried for three revolutions of the engine crankshaft. The reason behind this was to achieve the same pressure variations inside each exhaust pipe during the single revolution of the crankshaft. Table 6 shows the parameters of the node device that was used for computing purposes.

Table 6. The parameters of the node device.

Parameters of the Node Device	
Number of cores	4
Random-access memory [Gb]	32
Graphics processor unit memory [Gb]	0.5

With such computational restraints and such a low time step, the time needed for the calculation of the single revolution of the crankshaft was about 1.5 weeks.

Figure 7 shows the mass flow average pressure variations at the first-stage turbine inlet during the 3 revolutions of the crankshaft.

Figure 7 shows that for every turbine speed the pressure variations for each exhaust pipe were almost similar during the 3rd revolution of the crankshaft except for the 40,000 rpm case. The shapes of the pressure plot for each exhaust pipe were different in this case. For the 40,000 rpm case, the maximal pressure values during the 3rd revolution of the crankshaft changed from 485,000 Pa for the exhaust pipe 2 to 502,500 Pa for the exhaust pipe 5. However, such a difference was within the acceptable range. The minor changes can be observed between the 3rd and 2nd revolution of the crankshaft. However, based on the author's previous experiences, the results for the 4th revolution of the crankshaft were not presented as further changes did not exceed 1%. That is why the results were presented during the 3rd revolution of the crankshaft.

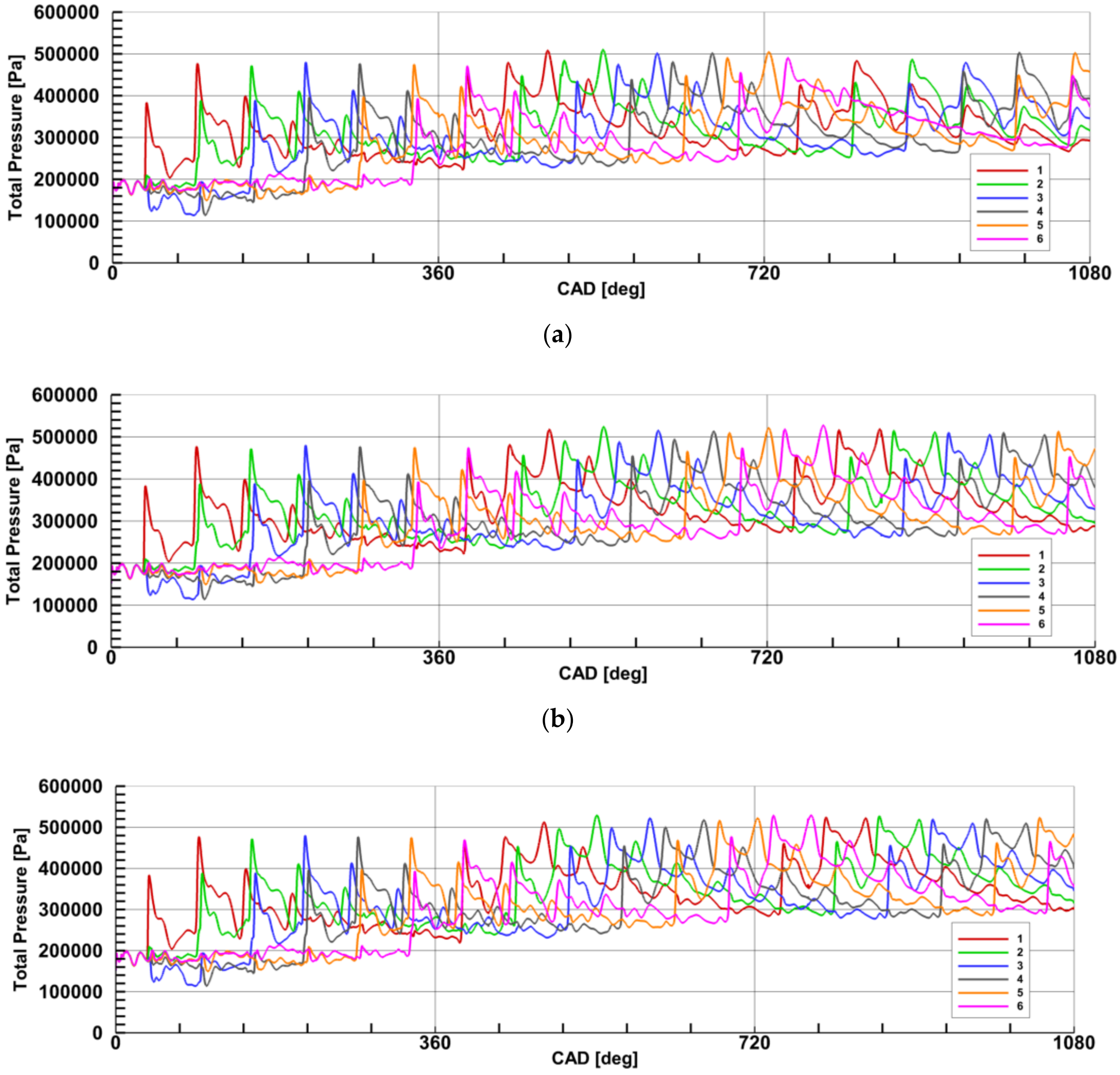

(**a**)

(**b**)

(**c**)

Figure 7. The mass flow average pressure variations at the turbine inlet at: (**a**) n = 40,000 rpm; (**b**) n = 50,000 rpm; (**c**) n = 60,000 rpm.

4. Model Validation

The numerical model was validated against the experimental data. The parameter used for the comparison between the real data and the predicted values is the root mean square error (RMSE). The RMSE gives the difference between the actual and the predicted values. The RMSE is calculated using the formula below:

$$\mathrm{RMSE} = \sqrt{\frac{\sum_{i=1}^{n}\left(X_{obs,i} - X_{model,i}\right)^2}{n}} \tag{14}$$

where, the $X_{obs,i}$ is the measured value, $X_{model,i}$ is the predicted value and n is the number of data points. For the measured and predicted values, the area-averaged total pressure at the outlet from the second-stage rotor was used. The validation results are shown in Figure 8 for the 60,000 rpm case during the three revolutions of the crankshaft.

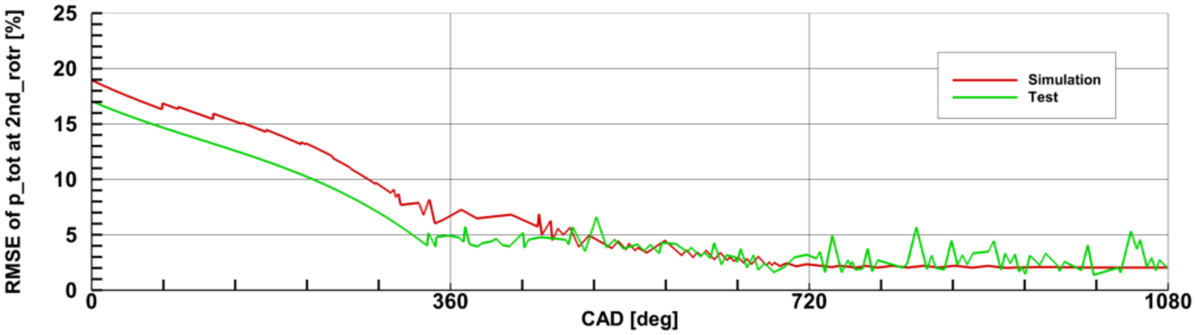

Figure 8. Numerical model validation against the experimental results using the RMSE parameter.

The RMSE of the total pressure for the numerical simulation fall within 2% for the 3rd revolution of the crankshaft. Such results are acceptable for validation purposes.

5. Results and Discussion

Figure 9 shows the plots of the area-averaged mass flow rate that was monitored in the Section 1-1 for three different turbine speeds. The plots were captured during the 3rd revolution of the crankshaft. For every turbine speed, the shapes of the pressure plots were almost similar and shifted by 60° crank angle degree (CAD). From Figure 8 one can see that the shape of the pressure plot of the exhaust pipe 6 during the exhaust phase differs from the rest of the pressure plots. This pressure plot comes from the 2nd revolution of the crankshaft because of the 60° CAD shift between the exhaust pulses. The shapes of the pressure plots of 40,000 rpm case were different when compared to the pressure plots of 50,000 rpm and 60,000 rpm cases. The dashed rectangle shows the deteriorated mass flow rate at the end of the pulse for every exhaust pipe. Such a phenomenon is shown in Figure 9 in much greater detail.

Figure 10 shows the mass flow rate and the total pressure of exhaust pipes 1 and 2 during the 3rd revolution of the crankshaft at three different turbine speeds.

From Figure 10 it can be seen that for 50,000 rpm and 60,000 rpm case the mass flow rate of the exhaust pipe 2 decreased between the 30° and 88° CAD and for the 40,000 rpm case, between the 37° and 96° CAD. This was associated with the increase of the mass flow rate inside the exhaust pipe 1 due to the opening of the exhaust valve. The lowest value of the pipe 2 mass flow rate was 0.084 kg/s at 41° CAD for 40,000 rpm, 0.092 kg/s at 31.6° CAD for 50,000 rpm and 0.094 kg/s at 32.1° CAD for 60,000 rpm. The pipe 2 exhaust valve opened at the 83° CAD for every case, this increased the mass flow rate. The interaction between the pipe 1 and pipe 2 mass flow rate after the opening of the pipe 1 exhaust valve was caused by the leakage between those pipes. As it can be seen from Figure 10a–c, between the opening of the pipe 1 exhaust valve and opening of the pipe 2 exhaust valve, first the exhaust pipe 2 operated in lower pressure values due to the end of the exhaust pulse, while the pressure inside the exhaust pipe 1 was at its peak values due to the opening of the exhaust valve. Although, the height of the tip clearance gap was only 3 mm, part of the exhaust gases passed from exhaust pipe 1 to exhaust pipe 2. Also Figure 10d–f show the velocity vectors at the state represented by the points A–C on the mass flow rate plots. The figures clearly show the leakage between the adjacent exhaust pipes with velocity vectors entering exhaust pipe 2 in the upstream direction. The lowest leakage was observed at point C for 60,000 rpm while the highest leakage was observed at point A for 40,000 rpm. At the 40,000 rpm rotor caused the lowest acceleration of the exhaust gases. That is why a larger portion of the exhaust gases passed through the tip clearance gap. However, no negative values of the pipe 2 mass flow rate were observed. This means that no backflow of the exhaust gases from pipe 1 to pipe 2 occurred.

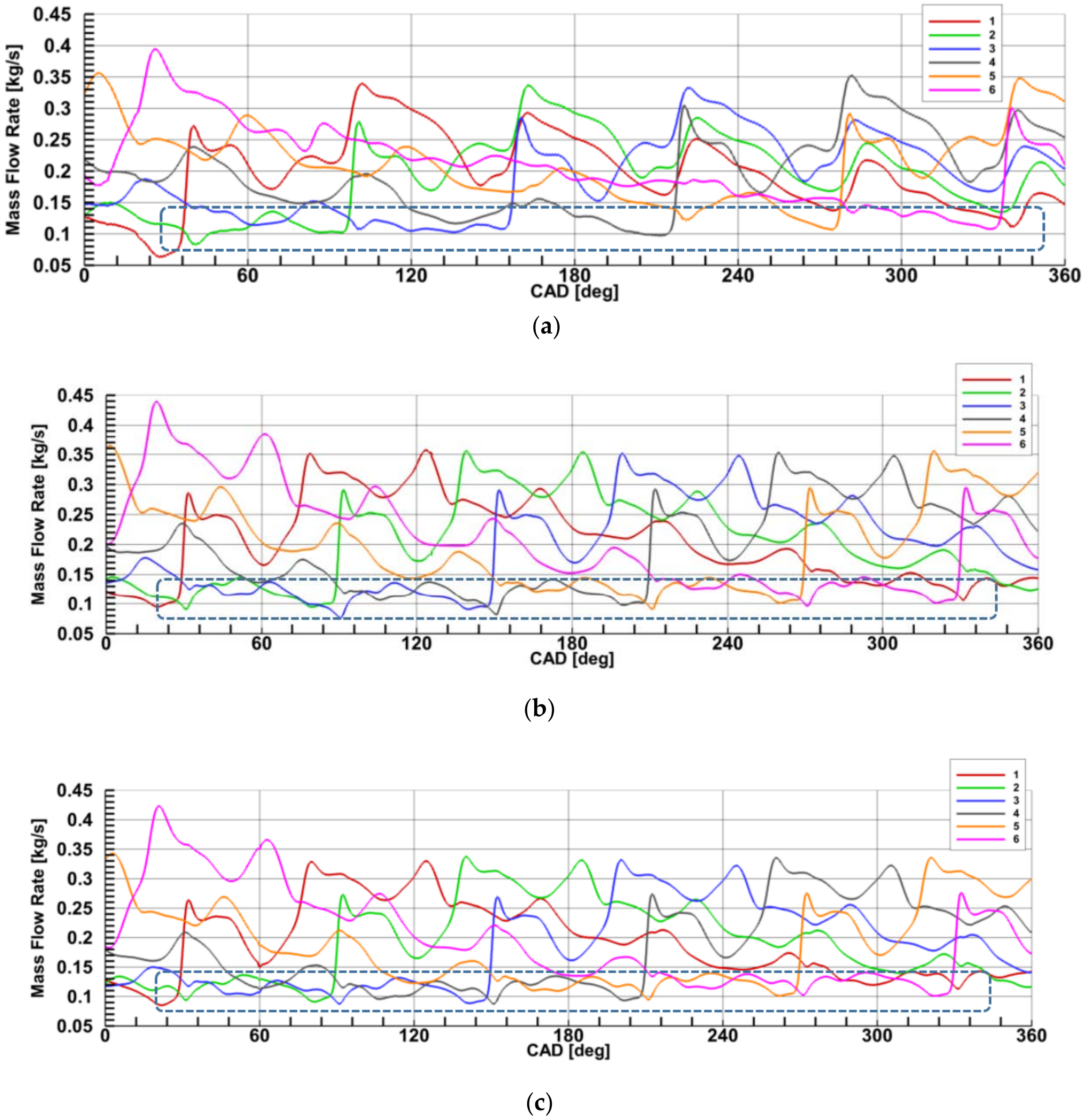

(**a**)

(**b**)

(**c**)

Figure 9. The area-average mass flow rate monitored at the Section 1-1 for: (**a**) n = 40,000 rpm; (**b**) n = 50,000 rpm; (**c**) n = 60,000 rpm.

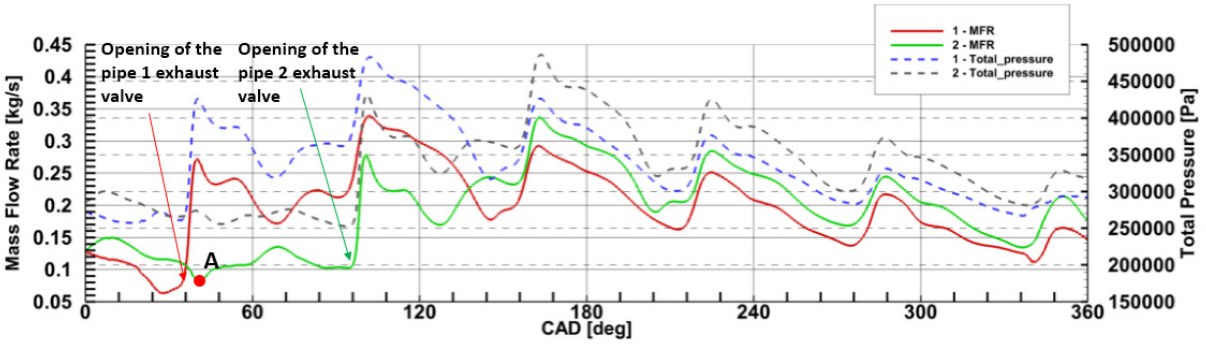

Figure 10. *Cont.*

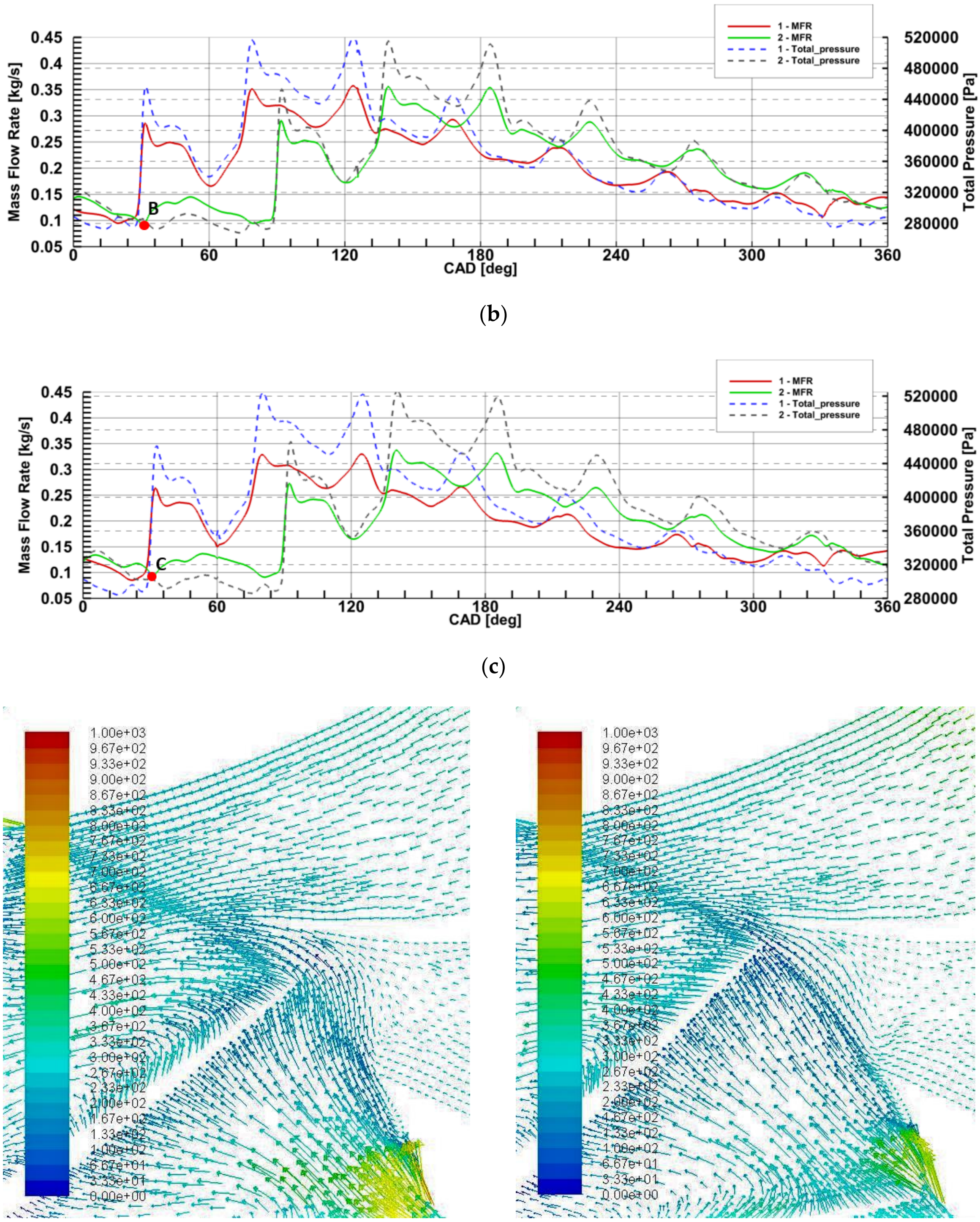

(**b**)

(**c**)

(**d**) (**e**)

Figure 10. *Cont.*

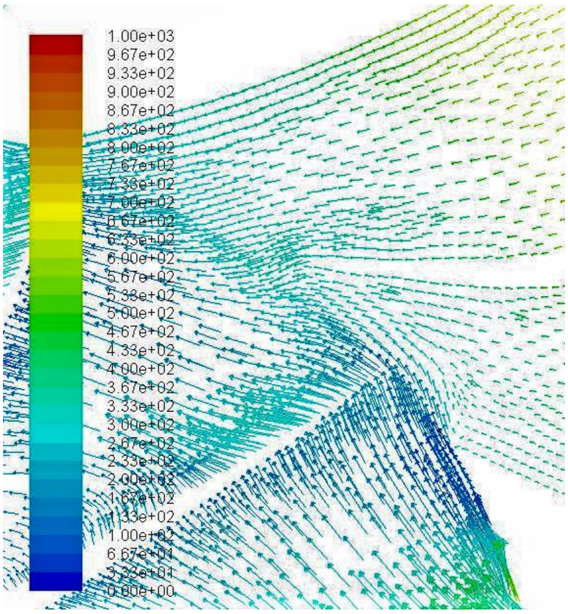

(**f**)

Figure 10. The plots of mass flow rate and total pressure monitored at the Section 1-1 of the exhaust pipes 1 and 2 for: (**a**) n = 40,000 rpm; (**b**) n = 50,000 rpm; (**c**) n = 60,000 rpm; and the corresponding velocity vectors at: (**d**) point A; (**e**) point B; (**f**) point C.

Figure 11 shows the pressure variations in the Section 1-1 during the 3rd revolution of the crankshaft for three different turbine speeds. For each turbine speed, the shapes of the pressure plots of each exhaust pipe were almost similar apart from exhaust pipe 6 which came from the 2nd revolution of the crankshaft. The pressure plots of each exhaust pipe were shifted by 60° CAD which is associated with the inlet boundary conditions shown in Figure 6. Figure 11d–f show the pressure contours and represent the turbine state at lines A–C respectively. By looking at the pressure contours, it can be seen that the highest pressure occurred inside the exhaust pipe 5.

Unlike the ordinary scroll turbine, the rotor was not supplied on the whole circumference during a single pulse. The rotor was supplied with exhaust gases only on the 1/6 of its circumference. However, due to the short intervals between pulses, it can be seen that the rotor was constantly supplied by the exhaust gases. The intersection of the pressure plots at the Section 1-1 during the 3rd revolution of the crankshaft for three turbine speeds is shown in Figure 12.

From Figure 12 it can be seen that during the 3rd revolution of the crankshaft the pressure was changing in a quasi-constant manner for every turbine speed. The average pressure values were 422,000 Pa, 460,000 Pa, and 476,000 Pa for 40,000 rpm, 50,000 rpm and 60,000 rpm case, respectively. Such differences between the pressure values for 40,000 rpm, 50,000 rpm and 60,000 rpm were caused by the increasing pressure ratio.

The pressure variations behind the first and second-stage rotor are shown in Figure 13a,b. One can see that the pressure at the outlet of the first-stage rotor was quasi-constant with minor fluctuations during the 3rd revolution of the crankshaft. The pressure at the Section 2-2 increased with the increase of the turbine rotational speed which was caused by the increase of the inlet pressure as shown in Figure 12. The pressure monitored at the Section 4-4 reached lower values with the increase of the turbine rotational speed. However, comparing the pressure plots from Figure 13a,b, one can assume that the pressure ratio of the second-stage rotor should further increase with the increase of the turbine rotational speed.

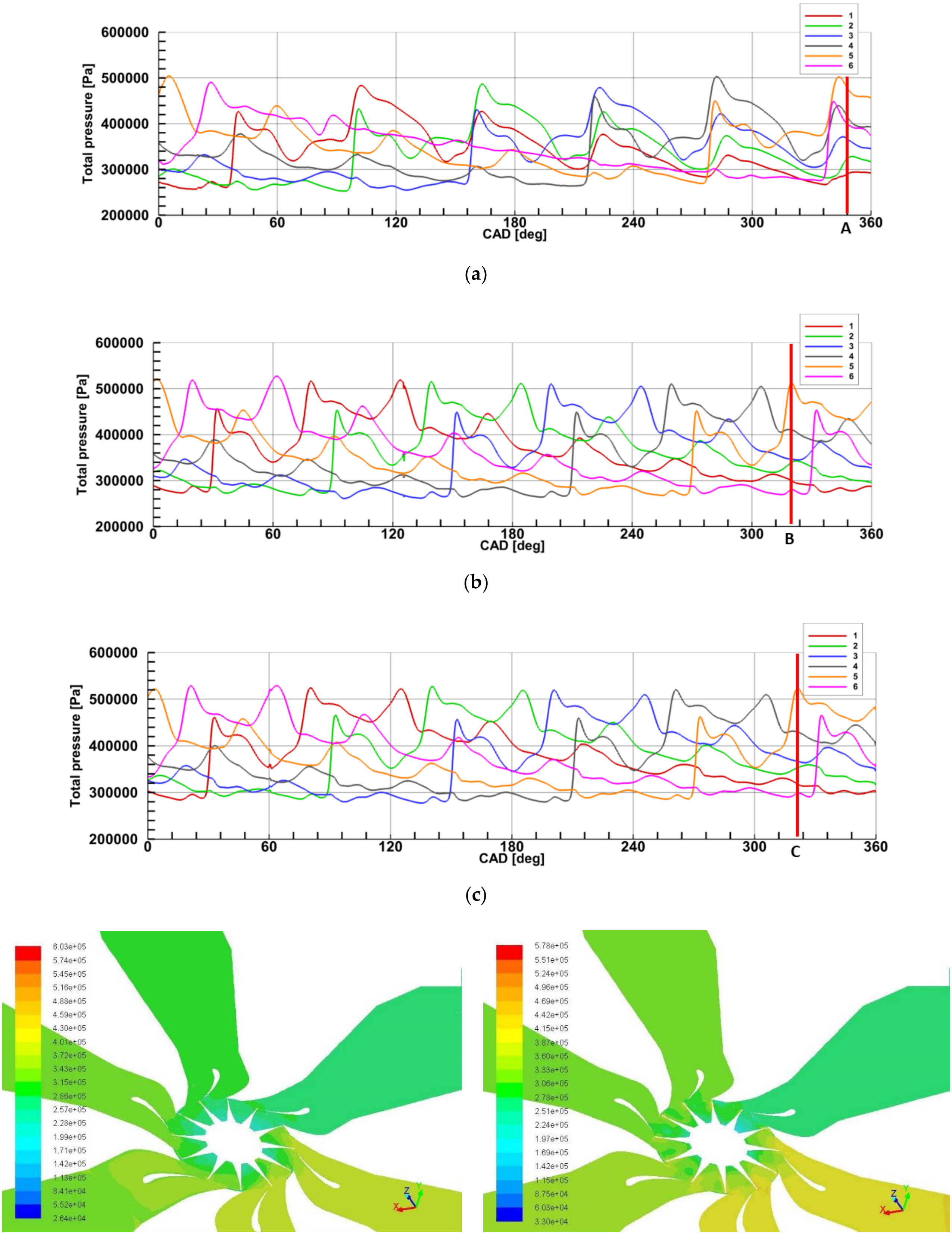

(**a**)

(**b**)

(**c**)

(**d**) (**e**)

Figure 11. *Cont.*

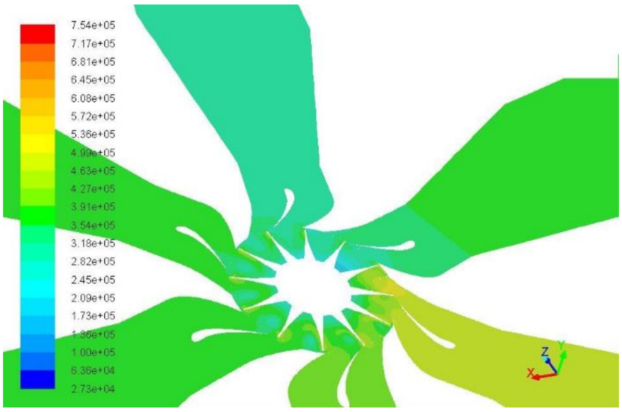

(**f**)

Figure 11. The plots of the total pressure monitored at the Section 1-1 during the 3rd revolution of the crankshaft for: (**a**) n = 40,000 rpm; (**b**) n = 50,000 rpm; (**c**) n = 60,000 rpm; and contours of the total pressure at the first-stage rotor during: (**d**) state A; (**e**) state B; (**f**) state C.

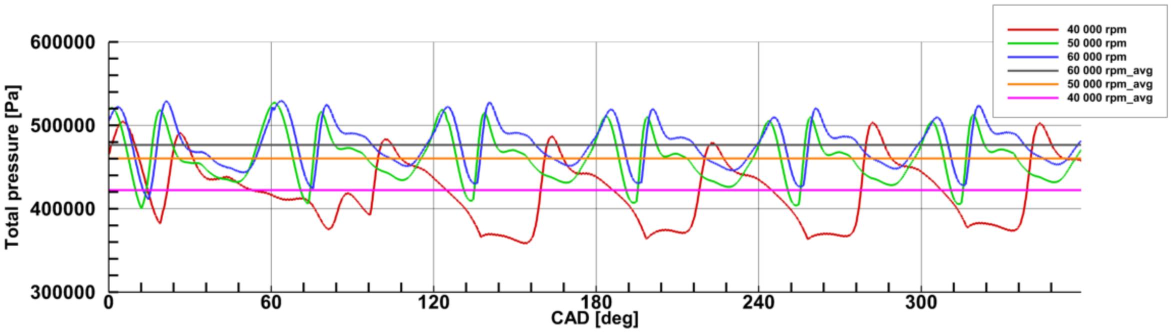

Figure 12. The inter Section of pressure plots monitored at the Section 1-1 for three different turbine speeds during the 3rd revolution of the crankshaft.

To investigate the pressure losses caused by the inter-stage pipes, the pressure values were monitored at the Sections 2.1-2.1 and 2.2-2.2. The results are shown in Figure 14 during the 3rd revolution of the crankshaft for three different turbine speeds. The instantaneous pressure losses were marked as percentage loss of the pressure monitored at the Section 2.1-2.1. The highest variations of the pressure losses can be seen in Figure 14a for 40,000 rpm case. The pressure losses, in this case, reached up to 12%. This might be caused by the lower acceleration of the exhaust gasses behind the first-stage rotor and vortices occurring inside the inter-stage pipes. For the turbine speed of 50,000 rpm and 60,000 rpm case, the pressure losses were the lowest. In those cases, the highest value of the instantaneous pressure losses reached up to 6%.

Figure 15 presents the plots of the pressure ratio for the first and second-stage rotor at three different turbine speeds during the 3rd revolution of the crankshaft. As it was mentioned previously, the pressure ratio of the first-stage rotor increased with the increase of the turbine speed. The same phenomenon was observed for the pressure ratio of the second-stage rotor. Higher changes in the pressure ratio values were observed at the first-stage rotor which was caused by the rapid pressure changes at the rotor inlet. On the other hand, changes in the pressure ratio for the second-stage rotor were lower. This was mainly a consequence of the quasi-constant character of the pressure behind the first and second-stage rotor. For the second-stage rotor, the pressure ratio fluctuations tend to be lower with the increase of the turbine speed. Such a phenomenon allows the second-stage rotor to operate in almost steady-stage conditions.

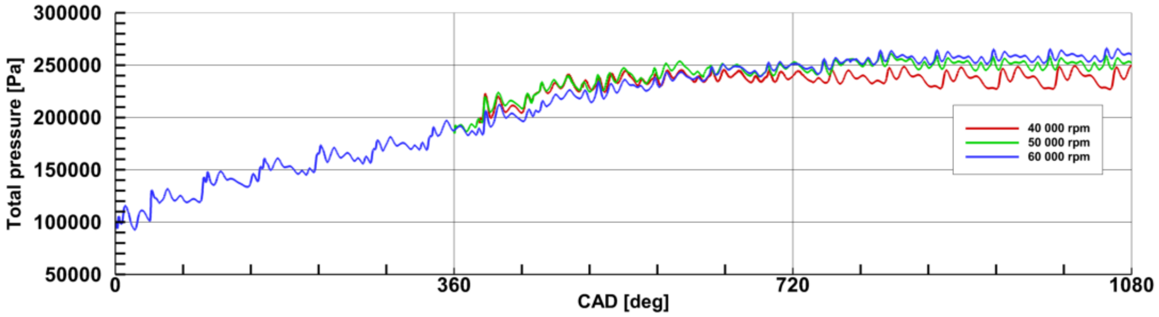

(**a**)

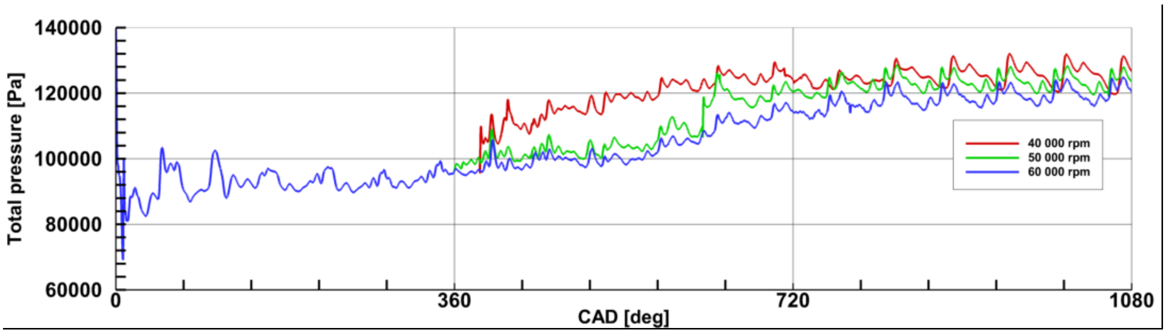

(**b**)

Figure 13. The pressure plots monitored for three different turbine speeds for the 3 revolutions of the crankshaft at: (**a**) the Section 2-2; (**b**) the Section 4-4.

The temperatures at the outlet from both rotors are shown in Figure 16. From Figure 16 one can see that the temperature behind the first and second-stage rotor became quasi-constant during the 3rd revolution of the crankshaft. It was found that, with the increase of the turbine speed, the temperature at the outlet increased. The reason for such a phenomenon is not known. A great difference between the temperatures at the Sections 2-2 and 4-4 can be observed which resulted in the recovery of the energy from the exhaust gases on the first and second-stage rotor. Figure 16c–e show the contours of the total temperature behind the first-stage rotor at state A for the 40,000 rpm, 50,000 rpm and 60,000 rpm case respectively. On the other hand, Figure 16f–h show the temperature contours behind the second-stage rotor at state B. It can be seen that the temperature drops behind the second-stage rotor. However, minor temperature changes can be seen behind the first stage rotor.

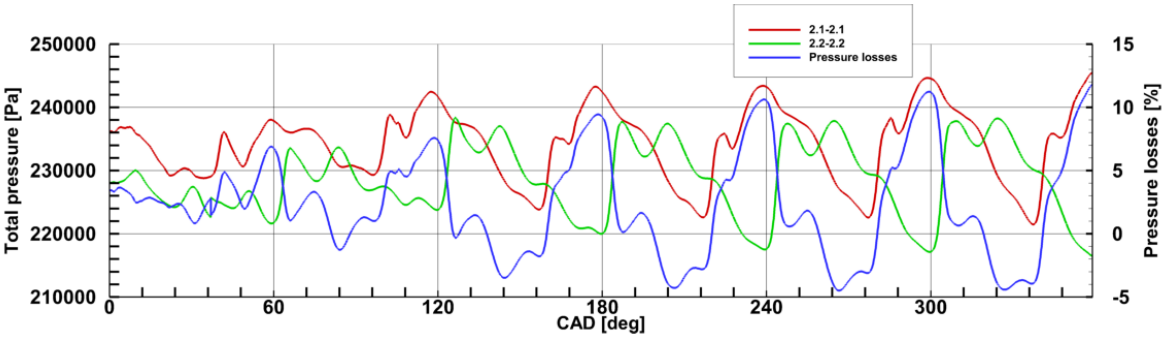

(**a**)

Figure 14. *Cont.*

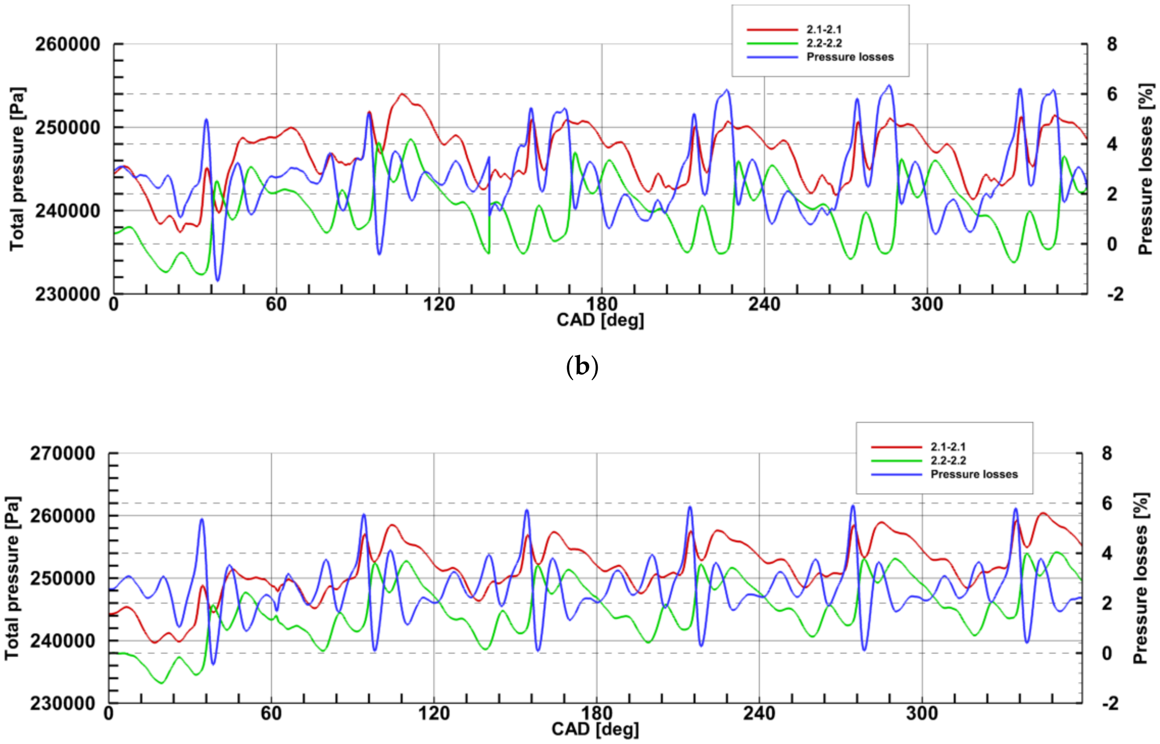

(**b**)

(**c**)

Figure 14. The pressure plots monitored at the Sections 2.1-2.1 and 2.2-2.2 with the percentage pressure losses between both Sections for: (**a**) n = 40,000 rpm; (**b**) n = 50,000 rpm; (**c**) n = 60,000 rpm.

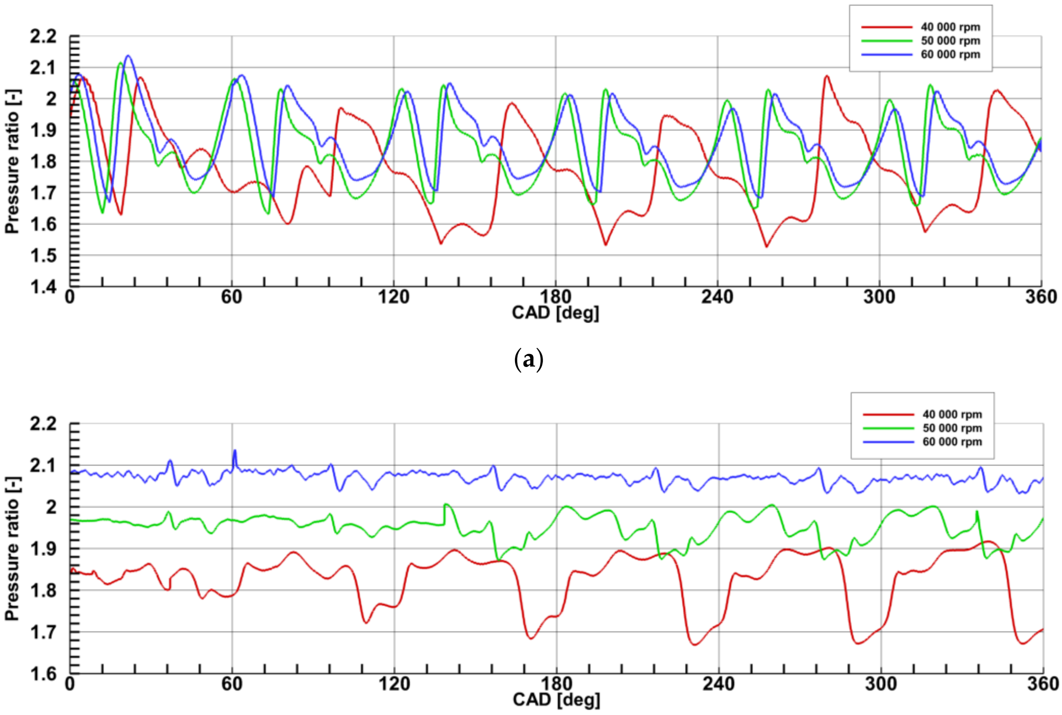

(**a**)

(**b**)

Figure 15. The pressure ratio at three different turbine speeds during the 3rd revolution of the crankshaft: (**a**) first-stage rotor; (**b**) second-stage rotor.

In Figure 17 one can see the variation of the total-static efficiency of the first and second-stage rotor during the 3rd revolution of the crankshaft for the three different turbine speeds. The efficiency during the 3rd revolution of the crankshaft was oscillating in a narrow range for every turbine speed. With the increase of the turbine speed, the efficiency of the first-stage rotor decreased. It was mainly caused by the presence of the second-stage rotor which increases the pressure behind the first-stage rotor and thus, lowers its pressure ratio. For the first-stage rotor, the highest efficiency was 0.89 for 40,000 rpm case. A completely different situation was observed for the efficiency values of the second-stage rotor. The efficiency values increased with the increase of the turbine speed. The highest efficiency value was 0.62 for the 60,000 rpm case. The high-efficiency values of the first-stage rotor were caused by the considerably higher inlet pressure and higher enthalpy drop. The efficiency of the complete two-stage system can be calculated using the formula below:

$$\eta_{t-s}^{T1-2} = \eta_{T1} * \eta_{T2} \tag{15}$$

Figure 18 shows the total-static efficiency of the complete two-stage system compared to the efficiency of the single-stage system with the same turbine model which was previously presented by the authors in [25].

The efficiency values of the two-stage system were higher than those in the single-stage system [25]. The average efficiency values of the two-stage system were 0.491 for the 40,000 rpm, 0.496 for the 50,000 rpm and 0.504 for the 60,000 rpm case. For the single-stage system, the efficiency values were 0.442, 0.475 and 0.484 for the 40,000 rpm, 50,000 rpm and 60,000 rpm case, respectively. Such differences lead to the conclusion that the two-stage system is more efficient than the single-stage system at the low turbine speed, thus at the low-load operating points of the engine however, the overall efficiency of the two-stage system is relatively low when compared to the modern scroll turbochargers.

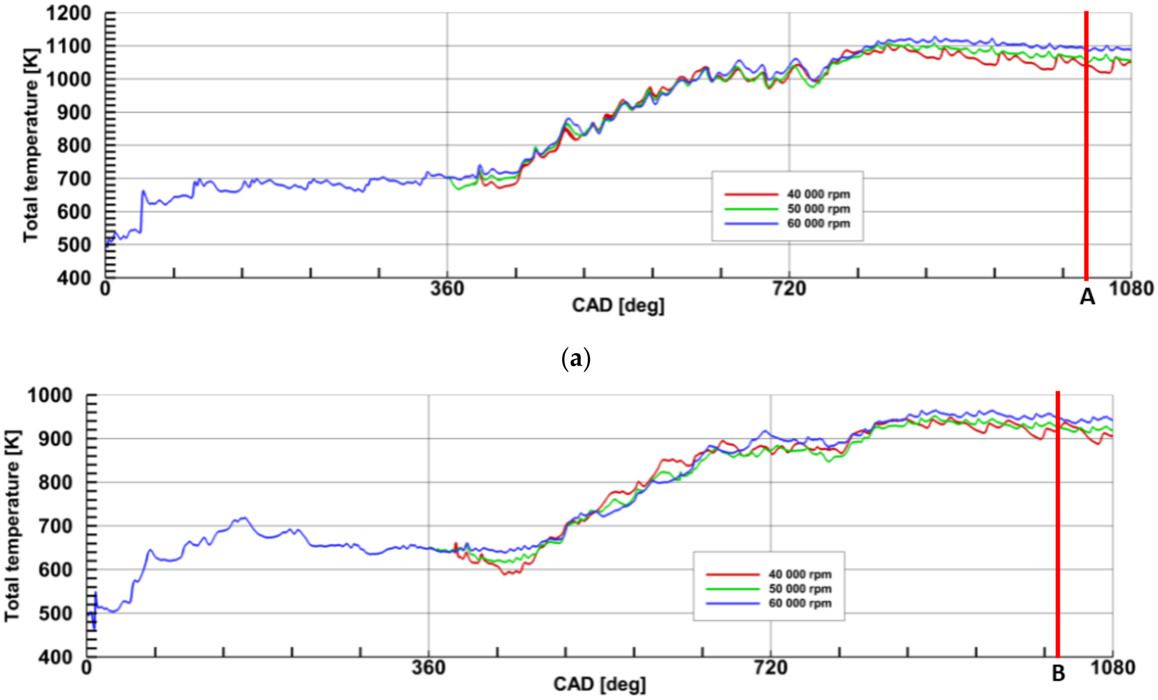

(**a**)

(**b**)

Figure 16. *Cont.*

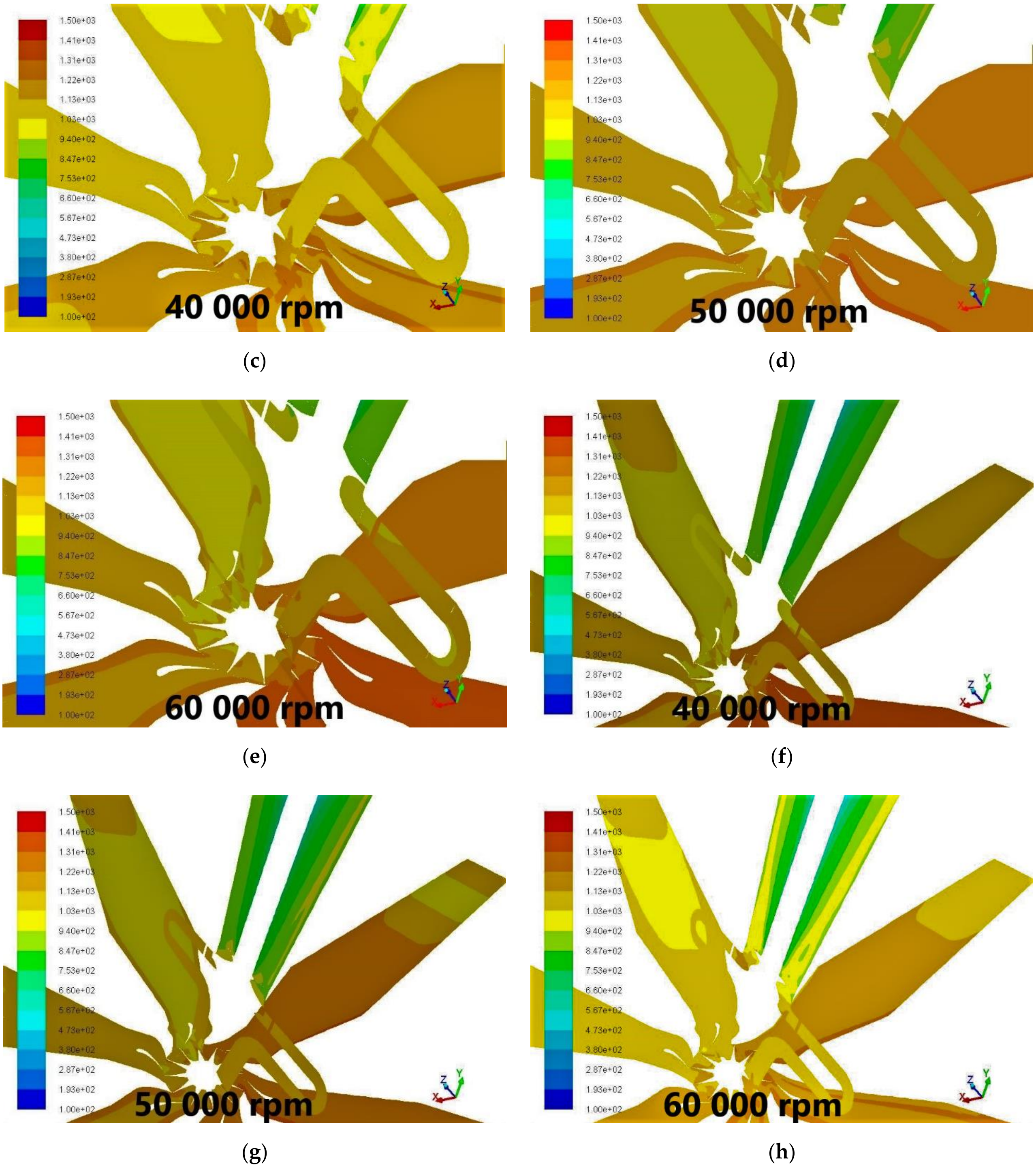

(**c**) (**d**)

(**e**) (**f**)

(**g**) (**h**)

Figure 16. The temperature plots for three different turbine speeds monitored at: (**a**) the Section 2-2; (**b**) the Section 4-4; and the contours of the total temperature behind the: (**c**–**e**) first-stage rotor at the state A; (**f**–**h**) second-stage rotor at the state B.

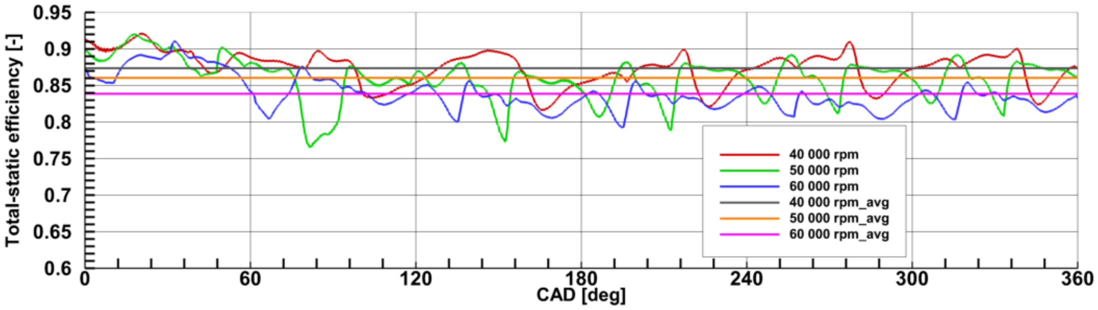

(**a**)

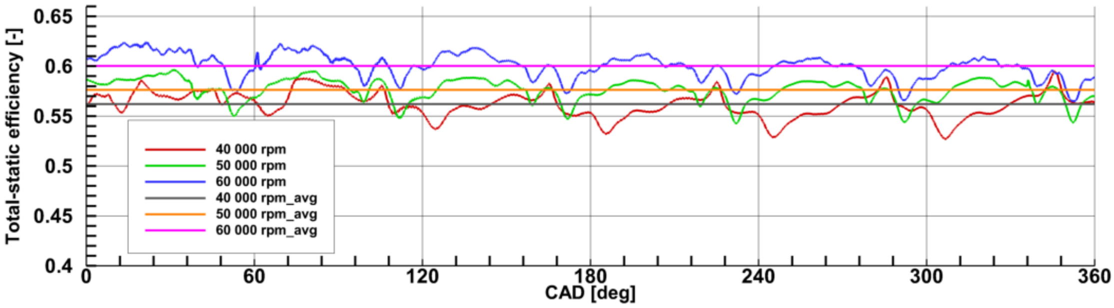

(**b**)

Figure 17. The total-static efficiency for three different turbine speeds, during the 3rd revolution of the crankshaft of the: (**a**) first-stage rotor; (**b**) second-stage rotor.

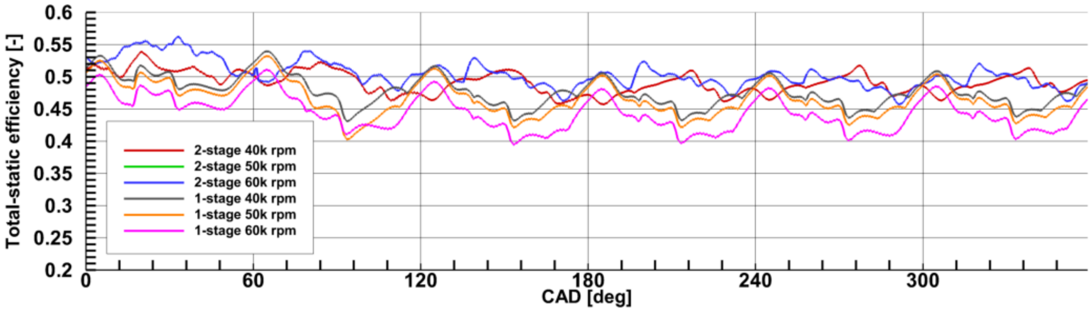

Figure 18. The total-static efficiency of the two-stage exhaust system and single-stage exhaust system for three different turbine speeds during the 3rd revolution of the crankshaft.

6. Adaptation of Two-Stage System for OP Engine

The recovered energy from the hot exhaust gasses will be transmitted back to the engine through turbocompounding. Such a conceptual scheme is shown in Figure 19.

Most of the turbocompound systems consist of the turbocharger turbine and free power turbine [26]. In this case, the end of the single-shaft, two-stage turbine system would be connected with the engine crankshaft with a gear train and fluid coupling. Such a concept has its drawback as the mechanical losses of the gear train and the fluid coupling are included [27–30]. Nowadays, most turbocompound solutions are focused on the generation of electrical power. The electric turbocompounding does not require a gear train or fluid coupling, and the generated energy could be used to supply other devices [31–34]. It was found that the electric turbocompounding is more efficient than the mechanical turbocompound especially for heavy-duty engines if the turbines are connected in parallel [35]. However, for this project, the series mechanical turbocompound system will be used. The type of gear train and fluid coupling is still a concern for future research.

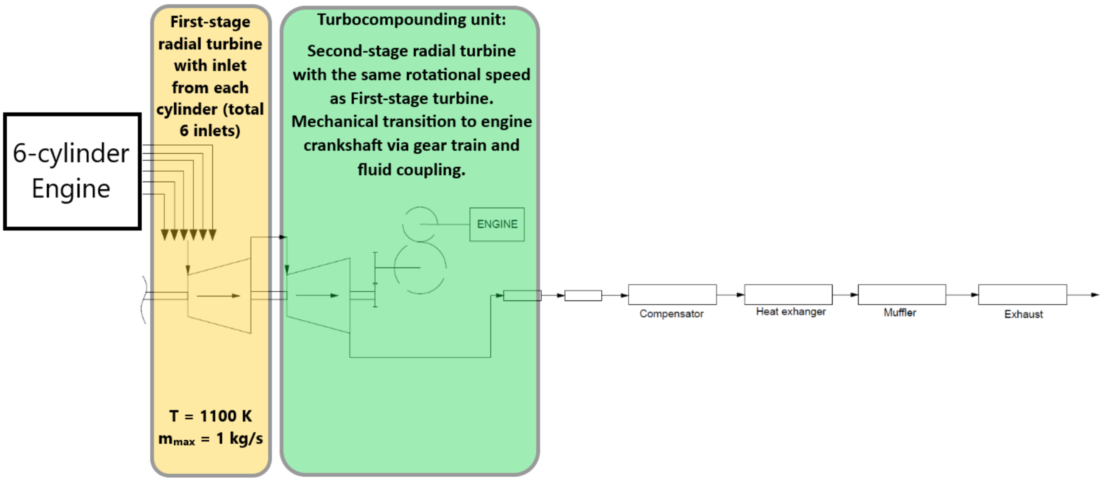

Figure 19. A schematic adaptation of two-stage turbine system for OP engine with turbocompounding unit.

7. Conclusions

The paper deals with the unsteady simulation of the two-stage, radial turbine under pulse-flow conditions. The novelty of this research was the development of a transient, 3-D simulation of the two-stage turbine with two rotors placed on a single shaft. The separation of the exhaust gases at the inlet of the first-stage rotor was also investigated. The simulations were carried out for the pulse-flow conditions at the inlet. The turbine wheel was scanned with the use of the 3-D scanner to create a virtual model. The same turbine model was used for the first and second-stage. The computational domain was generated using 3-D CAD software. The simulations were carried out using Ansys Fluent software with a small time step. The simulations lasted until the 3rd revolution of the crankshaft. Three different turbine speeds were investigated. The two-stage system was capable of recovering energy from the exhaust gasses. The temperature between the inlet to the first-stage rotor and behind the second-stage rotor dropped by about 100 K. Also, the total pressure values changed from about 450,000 Pa at the inlet of the first-stage rotor to 120,000 Pa behind the second-stage rotor. It was also found that despite the pulsatile operation of the two-stage system, the first-stage rotor was constantly supplied with exhaust gases. The pressure at the inlet to the first-stage rotor and behind the second-stage rotor was changing in a quasi-constant manner. The pressure changes decreased with the increase of the turbine speed. It was also found that the presence of the second-stage rotor limited the pressure behind the first-stage rotor and thus, limited its pressure ratio. That is why the total-static efficiency of the first-stage rotor decreased with the increase of the turbine speed. A great efficiency difference between the two-stage system and single-stage system at the low turbine speed was observed. This showed that such a system might be efficient at low-loads of the ICE. However, at the higher turbine speed, the efficiency difference between the two-stage system and single-stage system was lower and reached up to 2%. On the other hand, the two-stage system with newly designed housing provided proper separation between exhaust pulses. A relatively low leakage between the adjacent exhaust pipes was observed during the simulation. Also, no negative values of the mass flow rate were observed which meant that no backflow occurred during the simulation. The low total-static efficiency values of the two-stage system give room for improvement. However, for multicylinder engines, more than one scroll turbocharger needs to be used. Because of that, the exhaust system is more complex. On the other hand, with such a two-stage turbocharging system, the exhaust system would be easier to design. Such a system satisfies the demands of both the variable turbine geometry turbocharger and scroll turbocharger. The two-stage turbocharging system is a very promising device with its reduced leakage between the exhaust pipes and variable turbine geometry features. That is why further research will focus on the influence of the different positions of the second-stage nozzle vanes to control the backpressure in the exhaust system. The final milestone is the manufacturing of the prototype device with a two-stage expansion system and adjustable nozzle vanes at the second-stage. Such a system will be used in a 2-stroke, 6-cylinder OP engine which is being developed at the Warsaw University of Technology.

Author Contributions: Conceptualization, D.K., P.M.; Methodology, D.K.; Writing, D.K.; Supervision, P.M. Both authors have read and agreed to the published version of the manuscript.

Funding: This work is a part of Applied Research Programme of the National Centre for Research and Development within the scope of applied research in industry branches (programme path B), Badania wysokosprawnego silnika wykorzystującego technologię HCCI do zastosowań w energetyce rozproszonej” (GENEKO)-contract number PBS3/B4/16/2015.

Institutional Review Board Statement: Not applicable.

Informed Consent Statement: Not applicable.

Data Availability Statement: Not applicable.

Acknowledgments: The authors are pleased to acknowledge BorgWarner Poland company for their support in research.

Conflicts of Interest: The authors declare no conflict of interest.

Nomenclature

Notations	
w	Relative velocity
c	Absolute velocity
u	Linear velocity
p	Static pressure
p^*	Total pressure
T^*	Total temperature
ϕ	Vane flow coefficient
k'	Exhaust specific heat ratio
R'	Exhaust gas constant
Δh_{Tiz}	Turbine isentropic enthalpy drop
c_{iz}	Theoretical velocity during the isentropic expansion
ρ	The turbine reaction ratio
Δh_{Wiz}	The rotor isentropic enthalpy drop
I_{uT}	The expansion work of the rotor blades
η_{uT}	The expansion efficiency of the rotor blades
h^*	Total enthalpy
D	Diameter of the turbine
n	The rotational speed of the turbine
Subscripts	
0	Conditions before first-stage nozzle vanes
1	Conditions after first-stage nozzle vanes
2	Conditions after first-stage rotor
3	Conditions before second-stage rotor
4	Conditions after second-stage rotor
5	Conditions at the outlet

Abbreviations	
ICE	Internal combustion engine
3-D	Three-dimensional
ORC	Organic Rankine cycle
CFD	Computational fluid dynamics
AC	Alternating current
OP	Opposed piston (engine)
TE	Trailing edge
SA	Spalart-Allmaras turbulence model
CAD	Crankshaft angle degree

References

1. Tian, W.; Du, D.; Li, J.; Han, Z.; Yu, W. Establishment of a two-stage turbocharging system model and analysis on influence rules of key parameters. *Energies* **2020**, *13*, 1953. [CrossRef]
2. Chen, J.; Zhuge, W.; Zhen, X.; Zhang, Y. Investigation of influence of two-stage turbocharging system on engine performance using a pre-design model. In Proceedings of the ASME Turbo Expo 2013: Turbine Technical Conference and Explosion GT2013, San Antonio, TX, USA, 3–7 June 2013.
3. An, B.; Shiraishi, T. Development of variable two-stage turbocharger for passenger car diesel engines. *Mitsubishi Heavy Ind. Tech. Rev.* **2010**, *47*, 1–6.

4. Liu, R.; Zhang, Z.; Yang, C.; Jiao, Y.; Zhou, G.; Ma, J. Influence of altitude on matching characteristic of electronic-controlled pneumatic two-stage turbocharging system with diesel engine. *Proc. Inst. Mech. Eng. Part A J. Power Energy* **2021**, *235*, 94–105. [CrossRef]
5. Serrano, J.R.; Arnau, F.J.; Dolz, V.; Tiseira, A.; Lejeune, M.; Auffret, N. Analysis of the capabilities of a two-stage turbocharging system to fulfil the US2007 anti-pollution directive for heavy duty diesel engines. *Int. J. Automot. Technol.* **2008**, *9*, 277–288. [CrossRef]
6. Cui, Y.; Hu, Z.; Deng, K.; Wang, Q. Miller-cycle regulatable, two-stage turbocharging system design for marine diesel engines. *J. Eng. Gas Turbines Power* **2013**, *136*, 022201. [CrossRef]
7. Canova, M.; Chiara, F.; Rizzoni, G.; Wang, Y.-Y. Model-based characterization and analysis of diesel engines with two-stage turbochargers. *SAE Tech. Paper Ser.* **2010**, 1–12. [CrossRef]
8. Rinaldini, C.A.; Breda, S.; Fontanesi, S.; Savioli, T. Two-stage turbocharging for the downsizing of SI V-engines. *Energy Proced.* **2015**, *81*, 715–722. [CrossRef]
9. Sanaye, S.; Ghadikolaee, S.S.; Moghadam, S.A.A. A new method for optimum selection of two-stage turbocharger for heavy duty diesel engine. *Int. J. Heavy Veh. Syst.* **2015**, *22*, 42. [CrossRef]
10. Liu, R.; Zhang, Z.; Dong, S.; Zhou, G. High-altitude matching characteristic of regulated two-stage turbocharger with diesel engine. *J. Eng. Gas Turbines Power* **2017**, *139*, 094501. [CrossRef]
11. Li, H.; Shi, L.; Deng, K. Research on the power recovery of diesel engines with regulated two-stage turbocharging system at different altitudes. *Int. J. Rotating Mach.* **2014**, *2014*, 209084. [CrossRef]
12. Liu, Y.; Zhuge, W.; Zhang, Y.; Zhang, S. Numerical analysis of flow interaction of turbine system in two-stageturbocharger of internal combustion engine. *IOP Conf. Ser. Mater. Sci. Eng.* **2016**, *129*, 1–13. [CrossRef]
13. Vitale, S.; Pini, M.; Colonna, P. Multistage turbomachinery design using the discrete adjoint method within the open-source software SU2. *J. Propuls. Power* **2020**, *36*, 465–478. [CrossRef]
14. Panayides, C.; Pesyridis, A.; Saravi, S.S. Design of a sequential axial turbocharger for automotive application. *Energies* **2019**, *12*, 4433. [CrossRef]
15. Di Battista, D.; Gualtieri, A.; Cipollone, R. Turbocompound systems to recover energy in ICE. *Int. J. Eng. Innov. Technol.* **2014**, *3*, 249–257.
16. Kant, M.; Romagnoli, A.; Mamat, A.M.; Martinez-Botas, R.F. Heavy-duty engine electric turbocompounding. *Proc. Inst. Mech. Eng. Part D J. Automob. Eng.* **2014**, *229*, 457–472. [CrossRef]
17. Salehi, R.; Stefanopoulou, A.; Kiwan, R.; Martz, J. Design considerations for waste energy recovery with electric turbocompounding. In Proceedings of the ASME 2016 Dynamic Systems and Control Conference (DSCC2016), Minneapolis, MN, USA, 12–14 October 2016. [CrossRef]
18. Macek, J.; Vitek, O. Simulation of pulsating flow unsteady operation of a turbocharger radial turbine. *SAE Tech. Paper Ser.* **2008**. [CrossRef]
19. Spalart, P.; Allmaras, S. A one-equation turbulence model for aerodynamic flows. *Rech. Aerosp.* **1994**, *1*, 5–21.
20. Ebrahimi, M.; Roozbahani, M. Comparative investigation in a turbine blade passage flows with several different turbulence models. *Majlesi J. Mech. Eng.* **2011**, *4*, 39–45.
21. Popov, G.; Matveev, V.; Baturin, O.; Novikova, I.; Kolmakova, D.; Zubanov, V. Estimation of the Effect of 3D Grid Parameters on the Simulation of the Working Process of Axial Turbines. In Proceedings of the 8th International Conference on Simulation and Modeling Methodologies, Technologies and Applications: Simultech 2018, Porto, Portugal, 29–31 July 2018.
22. Abbass, A.; Sorour, M.; Teamah, M. Evaluation of different turbulence models and numerical solvers for a transonic turbine blade cascade. *Energy Power Sour.* **2014**, *1*, 17–30.
23. Deck, S.; Duveau, P.; D'Espiney, P.; Guillen, P. Development and application of Spalart–Allmaras one equation turbulence model to three-dimensional supersonic complex configurations. *Aerosp. Sci. Technol.* **2002**, *6*, 171–183. [CrossRef]
24. Chen, L.; Zhuge, W.; Zhang, Y.; Li, Y.; Zhang, S. Investigation of Flow Structure in a Turbocharger Turbine under Pulsating Flow Conditions. *SAE Int. J. Fuels Lubr.* **2008**, *1*, 1167–1174. [CrossRef]
25. Kozak, D.; Mazuro, P. Unsteady simulation of six-inlet pulsed-flow turbocharger turbine. *SAE Tech. Paper Ser.* **2020**, 1–9. [CrossRef]
26. Yin, Y.; Liu, Z.; Zhuge, W.; Zhao, R.; Zhao, Y.; Chen, Z.; Mi, J. Experimental study on the performance of a turbocompound diesel engine with variable geometry turbocharger. *Int. J. Fluid Mach. Syst.* **2016**, *9*, 332–337. [CrossRef]
27. Mysłowski, J.; Mysłowski, J. A trial to improve fuel-efficiency rates of a turbo-charged engine. *J. KONES Powertrain Transp.* **2008**, *15*, 375–380.
28. Piancastelli, L.; Frizziero, L. Turbocharging and turbocompounding optimization in automotive racing. *ARPN J. Eng. Appl. Sci.* **2014**, *9*, 2192–2199.
29. Mehta, J.; Charneski, J. A turbo compound internal combustion engine concept for UAV application. In Proceedings of the Propulsion and Energy Forum, Orlando, FL, USA, 27–29 July 2019.
30. Zhao, R.; Zhuge, W.; Zhang, Y.; Yin, Y.; Chen, Z.; Li, Z. Parametric study of power turbine for diesel engine waste heat recovery. *Appl. Therm. Eng.* **2014**, *67*, 308–319. [CrossRef]

31. Bin, A.; Padzillah, H.; Romagnoli, A.; Ricardo, B. A high performance low pressure ratio turbine for engine electric turbocompounding. In Proceedings of the ASME Turbo Expo 2011: Power for Land, Sea and Air, Vancouver, BC, Canada, 6–10 June 2011.
32. Bin, A.; Romagnoli, A.; Ricardo, B. Design and development of a low pressure turbine for turbocompounding applications. *Int. J. Gas Turbine. Propuls. Power Syst.* **2012**, *4*, 1–8.
33. Chiriac, R.; Chiru, A.; Condrea, O. New Turbo Compound Systems in Automotive Industry for Internal Combustion Engine to Recover Energy. *IOP Conf. Ser. Mater. Sci. Eng.* **2017**, *252*, 012089. [CrossRef]
34. Dellachà, J.; Damiani, L.; Repetto, M.; Prato, A.P. Dynamic model for the energetic optimization of turbocompound hybrid powertrains. *Energy Proced.* **2014**, *45*, 1047–1056. [CrossRef]
35. Teo, A.; Yahya, W.; Romagnoli, A.; Rajoo, S.; Noor, A. Effectiveness of series and parallel turbo compounding on turbocharged diesel engine. *J. Mech. Eng. Sci.* **2015**, *8*, 1448–1459. [CrossRef]